Fracturing in Wet Granular Media Illuminated by Photoporomechanics

Yue Meng, Wei Li, and Ruben Juanes

Phys. Rev. Applied **18**, 064081 — Published 27 December 2022

DOI: 10.1103/PhysRevApplied.18.064081

Fracturing in wet granular media illuminated by photoporomechanics

Yue Meng,[1] Wei Li,[1] and Ruben Juanes[1,*]

[1] *Massachusetts Institute of Technology, 77 Massachusetts Avenue, Cambridge, MA, USA*

(Dated: December 1, 2022)

Abstract

We study fluid-induced deformation and fracture of granular media, and apply photoporomechanics to uncover the underpinning grain-scale mechanics. We fabricate spherical photoelastic particles of 2 mm diameter to form a monolayer granular pack in a circular Hele-Shaw cell that is initially filled with a viscous fluid. The key distinct feature of our system is that, with spherical particles, the granular pack has a connected pore space, thus allowing for pore-pressure diffusion and the study of effective stress in coupled poromechanical processes. We inject air into the fluid-filled photoelastic granular pack, varying the initial packing density and confining weight. With our recently developed experimental technique, photoporomechanics, we find two different modes of fluid invasion: fracturing in fluid-filled elastic media (with strong photoelastic response), and viscous fingering in frictional fluids (with weak or negligible photoelastic response). We directly visualize the evolving effective stress field, and discover an effective stress shadow behind the propagating fracture tips, where the granular pack exhibits undrained behavior. We conceptualize the system's behavior by means of a mechanistic model for a wedge of the granular pack bounded by two growing fractures. The model captures the pore pressure build-up inside the stress shadow region, and the grain compaction in the annular region outside. Our model reveals that a jamming transition determines the distinct rheological behavior of the wet granular pack, from a friction-dominated to an elasticity-dominated response.

INTRODUCTION

Multiphase flow through granular and porous materials exhibits complex behavior, the understanding of which is critical in many natural and industrial processes. Examples include infiltration of water into the vadose zone [1], growth and deformation of cells and tissues [2], and geological carbon dioxide storage [3]. While fluid-fluid displacement in rigid porous media has been studied in depth, the understanding of the interplay between multiphase flow and granular mechanics remains an ongoing challenge [4]. In many granular-fluid systems, the powerful coupling among viscous, capillary, and frictional forces leads to a wide range of patterns, including desiccation cracks [5, 6], fractures [7–13], labyrinth structures [14], granular fingers [15–17], corals, and stick-slip bubbles [18]. An in-depth study of poromechanics behind these coupled solid-fluid processes is crucial to understanding a wide range of phenomena, including methane migration in lake sediments [19], shale gas production [20], and hillslope infiltration and erosion after forest fires [21].

While fracturing during gas invasion in fluid-saturated media has been studied extensively in experiments [7, 8, 10–13, 16, 22] and simulations [9, 17, 23–29], the underlying grain-scale mechanisms behind the morphodynamics and rheologies exhibited by deformable granular media remain poorly understood. To investigate the interplay between fluid and solid mechanics of granular media, we adopt a recently developed experimental technique, *photoporomechanics* [30], to directly visualize the evolving effective stress field in a fluid-filled granular medium during the fracturing process. The key idea behind our photoporomechanics technique is the manufacturing of residual-stress-free photoelastic particles (such as spheres or icosahedra) that allow for connectivity of the pore space, so that pore pressure can diffuse and one fluid can displace another even without grain motion. In an earlier study of root growth in photoelastic granular media, Barés et al. [31] manufactured cylindrical photoelastic particles with a groove on the edge to allow for roots to grow between adjacent grains and propagate deep inside the granular medium. This disc-with-groove geometry, however, would likely experience strong adhesion/friction with the walls of the Hele-Shaw cell, and it's a less realistic representation of granular materials than spherical particles. Given the importance of frictional forces on the morphological regimes of the granular pack [18, 22], here we focus on the impact of confining weight on the fracture patterns. We also adopt packing density as a control variable, which proves to be key to rheological and morphological transitions in granular-fluid systems [18, 28].

In this study, we uncover two modes of air invasion under different initial packing densities and confining weights: fracturing in fluid-filled elastic media, and viscous fingering in frictional fluids. We discover an effective stress shadow behind the propagating fracture tips, where the intergranular stress is low and the granular pack exhibits undrained behavior. In the annular region outside the fractured region, the mechanical response of the granular medium transitions from friction-dominated to elasticity-dominated. To explain the observed distinct rheological behavior, we propose a mechanistic model for a wedge between two fractures. Finally, we rationalize the emergence of fracturing across our experiments as a jamming transition.

MATERIALS AND METHODS

Following the fabrication process in [30], we produce photoelastic spherical particles with a diameter $d = 2$ mm (with 3.5% standard deviation) and a volumetric modulus $K_p = 1.6$ MPa. We inject air into a monolayer of photoelastic particles saturated with silicone oil ($\eta = 9.71$ Pa·s) in a circular Hele-Shaw cell [Fig. 1]. When particles are immersed in silicone oil, the friction coefficient between particles is $\mu_p = 0.2 \pm 0.06$, and the friction coefficient between the particle and the glass plate is $\mu_w = 0.05 \pm 0.02$. To observe the photoelastic response of the particles, we construct a dark-field circular polariscope by means of a white light panel together with left and right circular polarizers [32]. Vertical confinement is supplied by a weight, W, adding up the weights from a confining weight, a light panel, a polarizer, and a glass disk that rests on top of the particles. The free top plate with prescribed confining weight is a natural representation of the conditions that prevail in subsurface processes, where the vertical confining stress is constant and controlled by the depth of the geologic stratum. To allow the fluids (but not the particles) to leave the cell, the disk is made slightly smaller than the interior of the cell (inner diameter $L = 21.2$ cm), resulting in a thin gap around the edge of the cell. A coaxial needle is inserted at the center of the granular pack for saturation, fluid injection and pore pressure measurement. We conduct experiments in which we fix the air injection rate ($q = 100$ mL/min) and the syringe reservoir volume ($V_0 = 15$ mL). We use three linear variable differential transformers (LVDTs) to monitor the vertical displacement of the top plate. We adopt a dual-camera system to record bright-field (camera A) and dark-field (camera B) videos. For the sample preparation, the initial packing density (ϕ_0) of the granular pack is controlled by the total mass of particles (M_s), and is calculated in 2D through image analysis. Before the air injection, we take a bright-field photo of the granular pack and create a binary mask with an intensity threshold. We then calculate the initial 2D packing density (ϕ_0) by dividing the number of particle pixels by the total number of pixels in the circular Hele-Shaw cell. To study the impact of packing density and frictional force, we vary ϕ_0 from 0.78 to 0.84 (M_s = 37 to 40 g), and the confining weight W from 25 N to 85 N. The influence of the confining weight (W) on ϕ_0 is negligible ($< 0.2\%$).

To gain additional insight into the rheological behavior of the granular pack, we record the spatiotemporal evolution of the packing density and effective stress fields from the experiments. To construct the 2D packing density field, we create a binary mask, then detect particle positions by centroid finding in MATLAB, and compute the packing density at each particle position within a sampling radius $3d$ [33] by dividing the number of particle pixels by the total number of pixels within the sampling circle. We then construct the packing density field for all the particles in the granular pack. To construct the effective stress field, we retrieve the light intensity of the blue channel from dark-field images and convert it into the effective stress value. To obtain the conversion factor between light intensity and effective stress, we conduct a single-bead calibration that directly relates light intensity to inter-particle force F [30]. By computing the Cauchy stress tensor for the calibrated particle under the diametrical loading condition, we obtain the expression that relates the inter-particle force to the effective stress, $\sigma' = \frac{6F}{\pi d^2}$ [34]. After this conversion, we visualize the time evolution of the effective stress field from the dark-field images.

RESULTS AND DISCUSSION

In Fig. 2, we show the invasion patterns resulting from air injection for experimental conditions with the same confining weight (W = 25 N) and two different initial packing fractions (ϕ_0 = 0.84, 0.78). The invasion patterns at breakthrough—when the invading fluid first reaches the outer boundary—indicate two invasion regimes: (I) fracturing in fluid-filled elastic media, with strong photoelastic response [Fig. 2(a)], and (II) viscous fingering in frictional fluids, with weak or negligible photoelastic response [Fig. 2(b)]. A light intensity

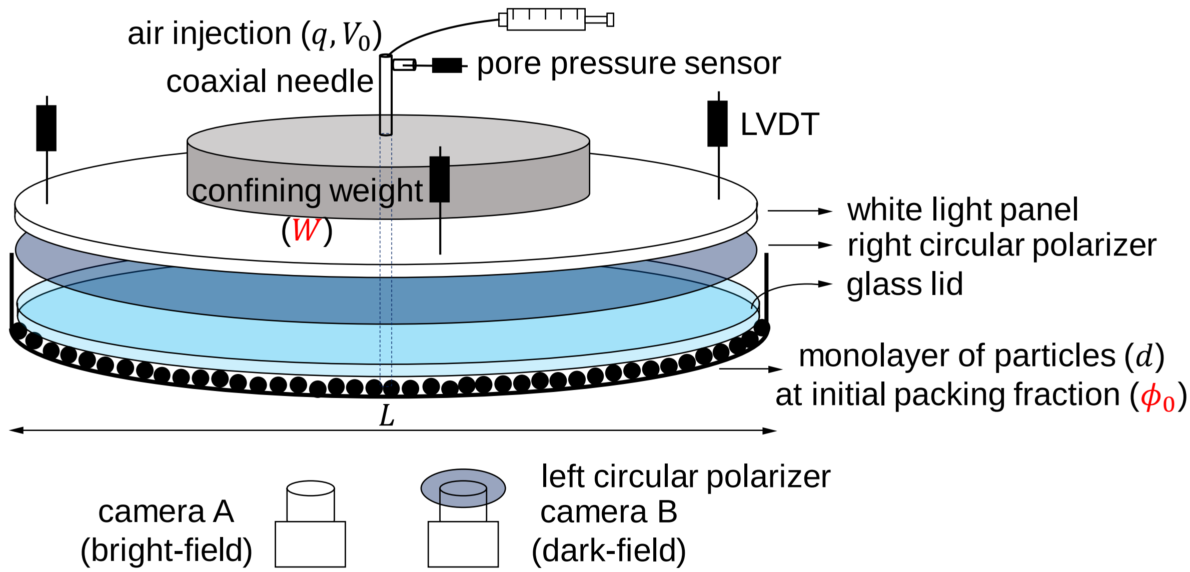

FIG. 1. Experimental setup: a monolayer of photoelastic particles (diameter d, initial packing density ϕ_0) saturated by silicone oil is confined in a circular Hele-Shaw cell (internal diameter L). Vertical confinement is supplied by a weight, W, adding up the weights from a confining weight, a light panel, a polarizer, and a glass disk that rest on top of the particles. The disk is slightly smaller than the cell to allow the fluids (but not particles) to leave the cell. Air is injected at a fixed flow rate q at the center of the cell with a coaxial needle, with the injection pressure monitored by a pore-pressure sensor. Three LVDTs are attached to the top of the light panel, capturing the vertical displacement of the top plate during the fracturing process. A white light panel, right and left circular polarizers form a dark-field circular polariscope. bright-field and dark-field videos are captured by cameras placed underneath the cell.

$I = 0.65$ in the blue channel of the dark-field images is adopted here as the threshold to differentiate between the two regimes. We analyze the time evolution of the air-oil interface morphology from bright-field images, and the rheological behavior of the granular pack from dark-field images (see supplemental videos corresponding to the conditions in Fig. 2 and see Appendix A for the complete visual phase diagram for a range of values of ϕ_0 and W). We compute the ratio between viscous and capillary forces in the experiments as the modified capillary number $\mathrm{Ca}^* = \eta q R/(\gamma h d^2)$ [22], where oil viscosity $\eta = 9.71$ Pa·s, injection rate $q = 100$ mL/min, cell radius $R = 10.6$ cm, interfacial tension $\gamma = 0.034$ N/m, cell height $h = 2$ mm, and particle diameter $d = 2$ mm, resulting in $\mathrm{Ca}^* = 6.3 \times 10^3$. Therefore the effect of capillarity is negligible and viscous effects are dominant in our experiments.

Regime I: Fracturing in fluid-filled elastic media. When particles have been densely packed initially, air initially invades into the granular pack by expanding a small cavity at the injection port, with the injection pressure P_{inj} ramping up during this period [Fig. 3(a)(d) for $\phi_0 = 0.84$]. The onset of fracturing in our cohesionless granular packs is determined by the viscous force from injection overcoming the frictional resistance between particles in the granular pack. Before fracturing, the injection pressure increases, and this pressure increase leads to an increased viscous force and, simultaneously, a decreased interparticle frictional force from the lifting of the top plate—a combination that results in the emergence and growth of fractures. Higher W results in higher peak pressure [Fig. 3(a)], and thus the fracture network becomes more vigorous with well-developed branches (see Appendix A). In this regime, the effective stress field exhibits a surprising and heretofore unrecognized phenomenon: behind the propagating fracture tips, an *effective stress shadow*, where the intergranular stress is low and the granular pack exhibits undrained behavior, emerges and evolves as fractures propagate [Fig. 2(a), right].

Regime II: Viscous fingering in frictional fluids. For granular packs with lower initial packing density ($\phi_0 = 0.78$), the system's rheology is akin to a frictional fluid [18, 28], as evidenced by the weak or negligible photoelastic response at breakthrough [Fig. 2(b), right]. The high-viscosity defending fluid inhibits the injected air from infiltrating into pore spaces [16]. The fluid-filled granular medium effectively behaves like a suspension [36], the morphology of which is dominated by the Saffman–Taylor instability [18, 37, 38].

The temporal evolution of the injection pressure and the vertical displacement of the top plate encode the information to help understand the interplay between particle movement and fluid-fluid displacement. At a high injection rate, the dynamics is dominated by the viscous response to the flow in the cell [22]. For all the confining weights, the injection pressure exhibits a peak followed by a decay, and a sharp drop corresponding to breakthrough of air at the cell boundary [Fig. 3(a)]. There are three ways to accommodate the injected air volume: compressing particles, driving defending fluid out of the cell, and lifting the confining weight to create extra vertical room. This last mechanism is favored under our experimental conditions, with injection pressure values $\sim$ 30 kPa. As shown in Fig. 3(b) where we plot the temporal evolution of the top plate's vertical displacement δh (normalized by the grain size d), the top plate is indeed lifted noticeably during fracturing: $\delta h/d = 5\%, 6\%, 8\%$ under W =25 N, 65 N, 85 N, respectively. For the fracturing experiments at

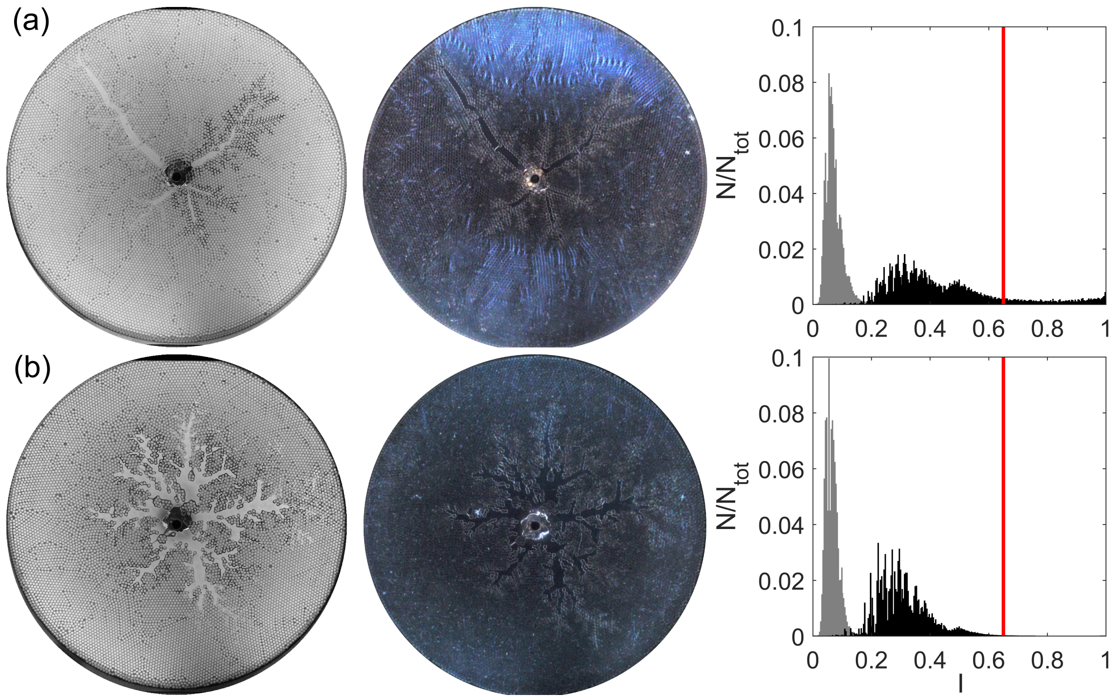

FIG. 2. Bright-field (left), dark-field (middle) images of the invading fluid morphology at breakthrough, and histogram (right) of light intensity of the blue channel of the dark-field image before air injection (in gray color), and at breakthrough (in black color), corresponding to two different initial packing densities ϕ_0, with confining weight $W = 25$ N. From the dark-field images that visualize the effective stress field, the invading morphology and rheology of the granular packs are classified as: (a) fracturing in fluid-filled elastic media, with strong photoelastic response ($I > 0.65$), $\phi_0 = 0.84$, or (b) viscous fingering in frictional fluids, with weak or negligible photoelastic response ($I < 0.65$), $\phi_0 = 0.78$. Behind the propagating fracture tips, the effective stress field exhibits an evolving "effective stress shadow", where the intergranular stress is low and the granular pack exhibits undrained behavior. See supplemental videos for the evolution of the morphology in each regime.

$\phi_0 = 0.84$, the initial cell height (h_0) is $0.98d, 0.96d, 0.95d$ under W =25 N, 65 N, 85 N, respectively (see Appendix B for detailed calculations). As W increases, a higher injection pressure is reached before the top plate is lifted [Fig. 3(a)], which stores a larger amount of air for fracturing. The invasion morphology at breakthrough [Fig. **??**] shows that, for larger W, a larger volume of air is injected into the cell by either fracture branches or pore invasion, both of which contribute to lifting the top plate. During air injection, while all the particles are in contact with both the top and bottom plates ($h(t) < d$), the confining weight is balanced by contact forces between particles and plates and the integrated pore pressure force across the Hele-Shaw cell. When the top plate is lifted to $h(t) > d$, the vertical component of the interparticle force is negligible and the confining weight is balanced by the integrated pore pressure force only.

We determine the spatiotemporal evolution of the packing density and effective stress fields as described in the Materials and Methods section [Fig. 3(e)(f)]. As fractures propagate, the pack is compacted ahead of the fracture tips, but exhibits a lower packing density around the fractures, reflecting the moving-average procedure that we use to determine it. In the fracturing experiments [Fig. **??**], we observe an asymmetric fracturing morphology with four to six fracture branches in total, and with one or two of them propagating faster and soon reaching the boundary. In an effort to characterize the rheological heterogeneity of the granular pack robustly and consistently across all the fracturing experiments, we define the fracture radius (r_{frac}) as the average distance from three representative fracture tips to the injection port, including both the long fractures that first reach the boundary and one or two shorter fractures near the injection port. As fractures propagate, the fracture radius increases, and the effective stress field exhibits marked rheological heterogeneity [Fig. 3(f)]. Behind the fracture tips ($r < r_{\mathrm{frac}}(t)$), we discover an *effective stress shadow*, where the intergranular stress is low and the granular pack exhibits undrained behavior. Ahead of the fracture tips ($r > r_{\mathrm{frac}}(t)$), particles in the annular region are compacted and behave elastically. For the annular region, this distinct rheological behavior from a frictional to an elastic response can be understood as a *jamming transition* [39, 40]. This is further evidenced by the temporal evolution of the averaged packing density and effective stress in the annular region outside fractures, ϕ_{out} and σ'_{out} [Fig. 3(c)], both of which rise above a background value at the critical point of mechanical stability (ϕ_c, σ'_c) [28, 39–41]. To show that fracturing is indeed the result of the transition to a solid-like rheological behavior, we analyzed the evolution of the packing fraction as a function of radial distance, $\phi(r)$, at different times, alongside the position of the fracture tip, for one of the fracturing experiments ($\phi_0 = 0.84, W = 25$ N; Fig. 4). The initial packing fraction is sufficiently close to the critical packing fraction ϕ_c that a relatively minor compaction elicits the formation and initial propagation of a fracture. The granular pack jams sometime between $t_{ii} \sim t_{iii}$, after which the fracture tip travels across the outer annular region, which is all above ϕ_c.

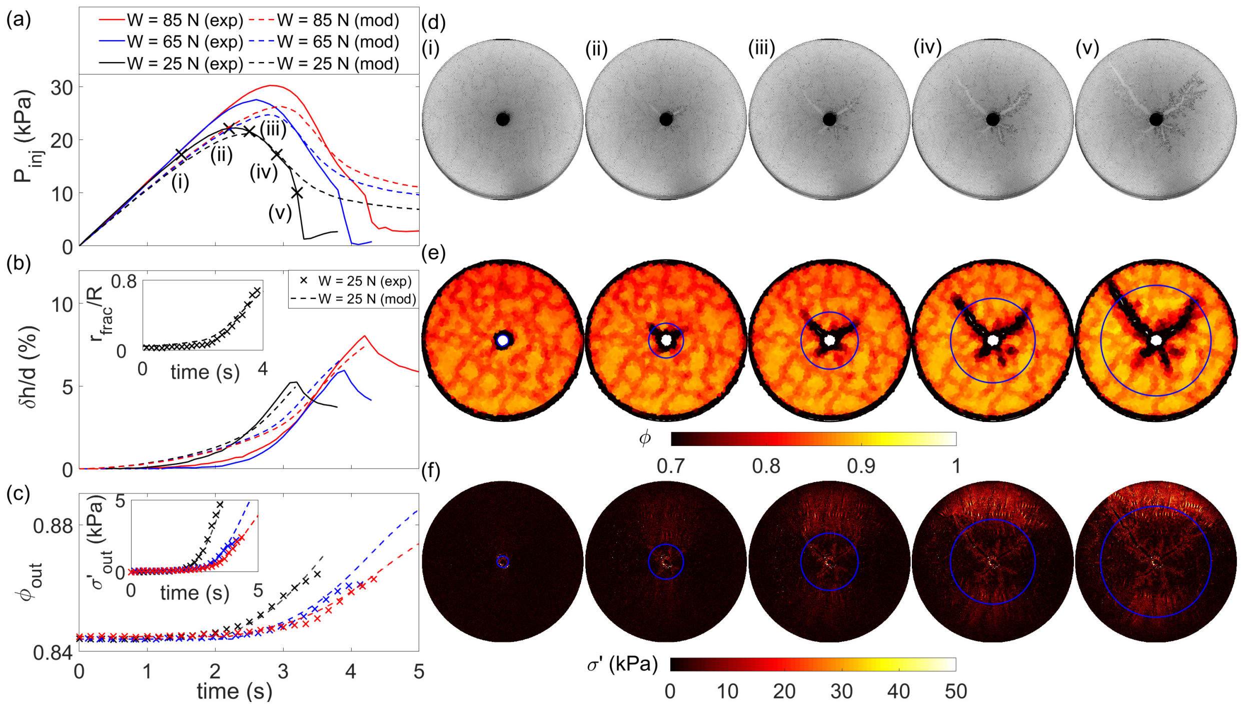

FIG. 3. Time evolution of (a) injection pressure P_{inj}, (b) normalized vertical displacement of the top plate $\delta h/d$, and (c) the averaged packing density ϕ_{out} in the annular region outside fractures for experiments with initial packing density $\phi_0 = 0.84$, and $W = 25$ N, 65 N, 85 N. Insets of (b), (c) show the time evolution of the normalized fracture radius r_{frac}/R, and the averaged effective stress σ'_{out} in the annular region outside fractures. The modeling results are plotted in dashed lines. For the experiment with $\phi_0 = 0.84$ and $W = 25$ N, a sequence of snapshots shows the time evolution of (d) interface morphology, (e) packing density field, and (f) effective stress field, where the radius of the blue circle represents the fracture radius (r_{frac}) averaged from three representative fracture tips.

Where does the effective stress shadow come from? And how does the rheology of a granular medium evolve during the fracturing process? To answer these questions, we hypothesize that the evolving effective stress shadow—the exhibited undrained behavior—stems from the buildup of pore pressure within the wedges of granular media between propagating fractures. The hypothesis emphasizes the strong coupling between fluid flow and solid mechanics underpinning the fracturing process.

To analyze the spatiotemporal evolution of the pore pressure, we develop a mechanistic model for a representative fracture wedge with an angle θ—a sector of the fluid-filled

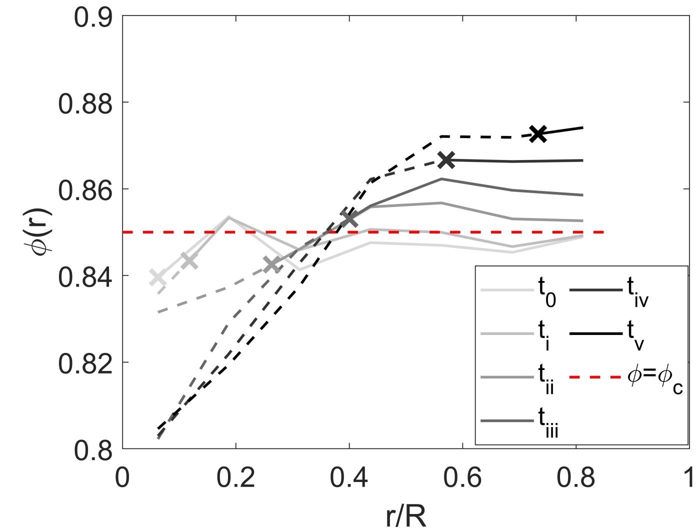

FIG. 4. Radial distribution of the packing fraction ($\phi(r)$) for the fracturing experiment with $\phi_0 = 0.84, W = 25$ N. The temporal evolution of $\phi(r)$ is plotted at six time instances, t_0 at $t = 0$, and $t_i \sim t_v$ in Fig. 3. The location of the fracture tip is indicated with the cross marker. The packing fraction distribution behind the fracture tip is plotted in dashed lines, and ahead of the fracture tip in solid lines. The red dashed line shows the packing fraction at the jamming transition, $\phi = \phi_c = 0.85$.

granular medium delineated by two fractures originating from the cell center [Fig. 5(a)]. We assume Hertz–Mindlin contacts [42] between particles and the plates, and calculate the initial vertical compression of the granular pack under the confining weight ($h_0 < d$). We model the fracturing process until breakthrough. The proposed model for a representative fracture wedge with an angle θ solves the time evolution of four unknowns: (1) the injection pressure $P_{\text{inj}}(t)$; (2) the height of the granular pack $h(t)$; (3) the length of the fracture $r_{\text{frac}}(t)$; and (4) the azimuthally dependent pore pressure field $p(r, \theta, t)$. The set of governing equations, along with their derivation and working modeling assumptions, is included in Appendix B.

The modeling results of P_{inj}, h and r_{frac} for different confining weights show good agreement with the experimental data [Fig. 3(a)(b)]. The time evolution of the pore pressure field during fracturing provides important clues to decipher the system's behavior [Fig. 5(c)]. The flow velocity field demonstrates a highly inhomogeneous distribution of the pore pressure gradient, which concentrates near the fracture tips [Fig. 5(b)]. The model captures the pressure build-up inside the fracture radius, resulting in the aforementioned "effective stress shadow", a region in which the granular pack is under near-undrained conditions. These fluidized particles in the stress shadow lead to grain compaction in the annular region outside, which helps explain the distinct rheological behavior from a frictional to an elastic response [Fig. 5(a)].

With the insights from the pore pressure model, we expect a different fluid-flow behavior in the loose and dense regions of the granular pack: a granular–fluid mixture behind the fracture tips, and an elastic medium ahead of the fracture tips. The homogeneous granular pack assumption in the pressure model (Appendix B) does not reflect the disparate rheology. For the rheology model, we take an effective permeability k' [43] and viscosity η' [36] for the granular-fluid mixture within the fracture radius and approximate the number of particles $N_{\delta t}$ entering the annular region within a timestep as $N_{\delta t} = (v_p \delta t/d) \cdot [r_{\mathrm{frac}}(t)\theta/d]$, with $v_p = -(k'/\eta')(\partial p/\partial r)|_{r=r_{\mathrm{frac}}(t)}$, where v_p is the particle flow velocity at the fracture radius. We update the two-dimensional packing density in the annular region as

$$\phi(t+\delta t) = \phi(t) + \frac{N_{\delta t}\frac{\pi d^2}{4}}{\frac{1}{2}(R^2 - (r_{\mathrm{frac}}(t))^2)\theta}. \tag{1}$$

To infer the effective stress from the packing density, we adopt the power-law constitutive relationship $\sigma' - \sigma'_c = K\left\langle \frac{\phi-\phi_c}{\phi_c} \right\rangle^{\psi}$ [39, 40, 44–46]. The modeling results of $(\phi(t),\ \sigma'(t))$ in the annular region agree well with the experiments [Fig. 3(c)], capturing both the pore pressure evolution and rheology of the granular medium. A detailed account of the modeling parameters is included in Appendix B.

To explore the rheological properties of the granular medium in the annulus, we conduct the jamming transition analysis for the fracturing experiments. We determine the jamming transition ϕ_c from the time evolution of the effective stress σ' as the intersection of two straight lines: one fitting the response of the background state, and one fitting the asymptotic behavior in the highly compacted state [28, 40, 47] [Fig. 6(a)]. We find that ϕ_c lies in the range 0.83–0.85 for the fracturing experiments [Fig. 2(a), and regime I in Appendix A], with higher ϕ_c corresponding to denser granular packs. The experimental value of ϕ_c is consistent with the theoretical prediction that the system jams at the random close packing density $\phi_c \approx \phi_{\mathrm{rcp}} \approx 0.84$ [28, 48–50]. We synthesize the elastic response of the system by plotting the effective stress against the packing density, showing that, above ϕ_c, σ' follows a power-law increase, $\sigma' - \sigma'_c \sim (\phi - \phi_c)^{\psi}$, with the exponent ψ in the range 1.1–1.5 [Fig. 6(b)]. As

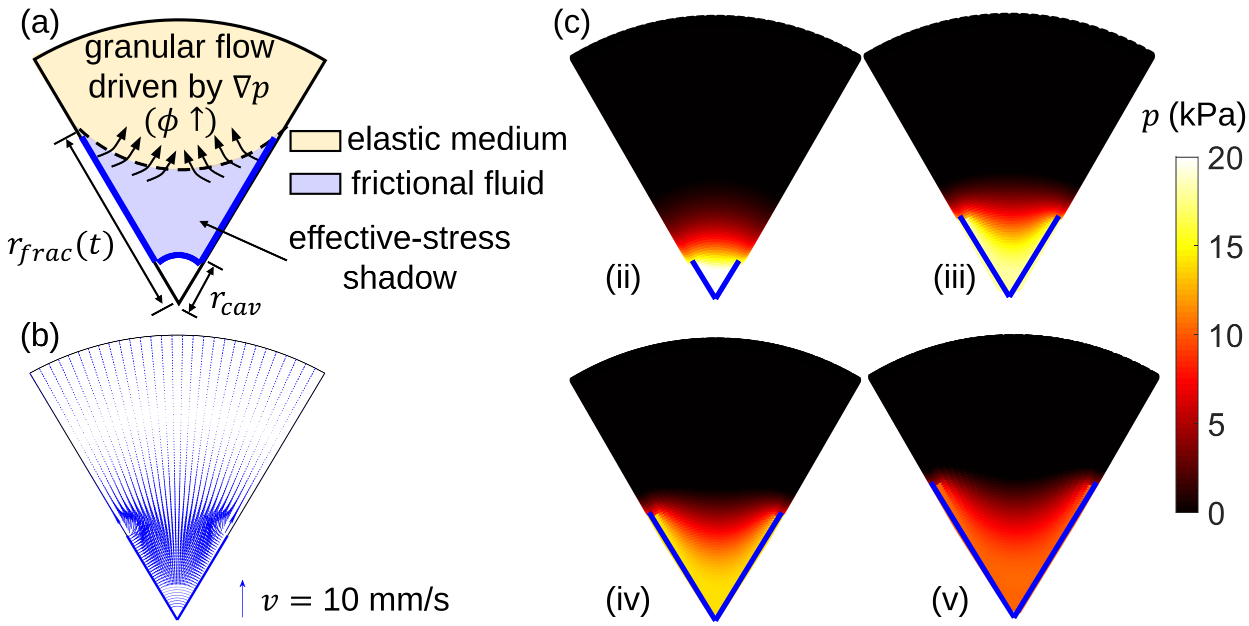

FIG. 5. A mechanistic model on fracturing that explains the effective stress shadow observed in experiments. (a) Schematic of the model setup for a fracture wedge with an angle $\theta = 60°$. The granular flow driven by the concentrated pore pressure gradient within fracture tips keeps compacting particles in the annular region outside, leading to its increase in packing density and a rheological transition from frictional flow to elastic medium. (b) Modeled flow velocity field at time instance (iii) in Fig. 3(a). (c) Sequence of snapshots showing the time evolution of the modeling pore pressure field. Modeling conditions: $\phi_0 = 0.84$, $W = 25$ N, $q = 100$ mL/min, and $V_0 = 15$ mL.

confirmed in previous studies [28, 39, 40, 44, 45], the value of ψ lies between the value for linear ($\psi = 1.0$) and Hertzian contacts ($\psi = 1.5$). In our stress–strain diagram [Fig. 6(b)], the elastic response in the annular region indicates a value of $K \sim 200$ to 300 kPa, which is close to the value measured in separate experiments [30]. Ideally, the parameters in the constitutive relation (K, ψ) would be the same for all the experiments, reflecting the material's elastic behavior after the jamming transition. In the experiments, though, this is not the case, and the coefficients in the power law exhibit some variability in part at least due to the asymmetric fracturing morphology and the inhomogeneous distribution of the packing fraction and effective stress fields ahead of the fracture tips. In an effort to characterize the rheological heterogeneity of the granular pack more robustly, in our mathematical model we define the fracture radius (r_{frac}) as the averaged distance from three representative fracture tips to the injection port.

CONCLUSIONS

In summary, we have studied the morphology and rheology of injection-induced fracturing in wet granular packs via a recently developed experimental technique, photoporomechanics, which extends photoelasticity to granular systems with a fluid-filled connected pore space [30]. Experiments of air injection into photoelastic granular packs with different initial packing densities and confining weights have led us to uncover two invasion regimes: fracturing in fluid-filled elastic media, and viscous fingering in frictional fluids. Visualizing the evolving effective stress field using photoporomechanics, we discover that behind the fracture tips, an *effective stress shadow*—where the intergranular stress is low and the granular pack exhibits undrained behavior—evolves as fractures propagate. With a mechanistic model for a fracture wedge, we capture the fluid pressure build-up inside the shadow region. We develop a rheology model that explains both the effective stress shadow behind the fracture tips, and the distinct rheological behavior from a frictional to an elastic response for the granular medium outside the fractures. Finally, we rationalize the emergence of fracturing across our experiments as a jamming transition initially proposed in the context of coupled pore-network/discrete-element models [28].

Our study paves the way for understanding the mechanical and fracture properties of porous media that are of interest for many field applications, including plant root growth in granular material [31, 51], powder aggregation [52], rock mechanics [53], soil rheology [54], and geoengineering [55]. We demonstrate that photoporomechanics serves as a promising technique to study coupled fluid-solid processes in granular media [4] and may provide fundamental insights on specific applications, including energy recovery [56], gas venting [57], and geohazards [58].

Y.M. and W.L. contributed equally to this work. This work was supported by the U.S. Department of Energy (Grant No. DE-SC0018357) and the U.S. National Science Foundation (Grant No. CMMI-1933416).

Appendix A: The Complete Visual Phase Diagram of Invading Fluid Morphology at Breakthrough

Figure 7 shows the complete visual phase diagram of invading fluid morphology for a range of values of ϕ_0 and W.

Appendix B: Mathematical Model of Coupled Fluid Pressure and Granular Mechanics

We develop a mechanistic model for a representative fracture wedge with an angle θ_0. We assume Hertz–Mindlin contacts [42] between particles and the plates, and calculate the initial vertical compression of the granular pack under the confining weight ($h_0 < d$). We model the fracturing process until breakthrough of the injected fluid. The model solves the time evolution of four unknowns: (1) the injection pressure $P_{\mathrm{inj}}(t)$; (2) the height of the granular pack $h(t)$; (3) the length of the fracture $r_{\mathrm{frac}}(t)$; and (4) the azimuthally dependent pore pressure field during fracturing, $p(r, \theta, t)$.

Governing equations

1. We assume fluid flowing in a homogeneous porous medium of uniform packing density (ϕ_{3d}), and time dependent uniform thickness ($h(t)$), in an azimuthally dependent manner. We perform a mass balance on an annulus sector between r and $r + \delta r$, θ and $\theta + \delta\theta$ (Fig. 8) for the incompressible defending fluid (silicone oil):

$$\rho_f(v_r r\delta\theta h - v_{r+\delta r}(r+\delta r)\delta\theta h + v_\theta \delta r h - v_{\theta+\delta\theta}\delta r h) = \frac{\partial(\rho_f r\delta r\delta\theta h(1-\phi_{3d}))}{\partial t} \quad \text{(B. 1)}$$

where ϕ_{3d} is the three-dimensional packing density of the granular pack, which is computed as the ratio between the volume of particles, and the cell volume saturated with the defending silicone oil. Before the air injection, $\phi_{3d} = \frac{V_s}{V_t} = \frac{M_s/\rho_s}{\pi R^2 h_0}$, where M_s and ρ_s are the mass and density of photoelastic particles in a granular pack, respectively. The initial cell height, h_0, is calculated from the confining weight by assuming Hertzian contacts between the particles and the glass plate. We estimate the 3D packing density before air injection and also at breakthrough, a calculation that shows a negligible difference between the two values. Therefore, in the model, we take the 3D packing fraction as a constant calculated with the initial cell height, $\phi_{3d,0}$. Dividing the equation by $\rho_f \delta r \delta\theta$, and letting $\delta r \to 0$, $\delta\theta \to 0$:

$$-\frac{\partial(v_r r h)}{\partial r} - \frac{\partial(v_\theta h)}{\partial\theta} = \frac{\partial(rh(1-\phi_{3d}))}{\partial t}, \tag{B. 2}$$

Combining with Darcy's law for the fluid velocity, we obtain:

$$\frac{\partial(rh\frac{k}{\eta}\frac{\partial p}{\partial r})}{\partial r} + \frac{\partial(\frac{h}{r}\frac{k}{\eta}\frac{\partial p}{\partial\theta})}{\partial\theta} = \frac{\partial(rh(1-\phi_{3d}))}{\partial t}, \tag{B. 3}$$

where k is the permeability of the granular pack and η is the viscosity of the defending fluid. We assume ϕ_{3d}, k, η to be constant in space and time. We then obtain the pressure diffusion equation for the defending fluid (silicone oil) in cylindrical coordinates as follows:

$$\frac{kh}{\eta}\left(\frac{\partial^2 p}{\partial r^2} + \frac{1}{r}\frac{\partial p}{\partial r} + \frac{1}{r^2}\frac{\partial^2 p}{\partial\theta^2}\right) = (1-\phi_{3d})\frac{\partial h}{\partial t}, \tag{B. 4}$$

2. Conservation of mass for the total air in the system:

$$P_{\text{inj}}(t)(V_0 - qt + V_{\text{air}}(t)) = P_0(V_0 + \pi r_0^2 h_0), \tag{B. 5}$$

$$V_{\text{air}}(t) = \pi r_0^2 h(t) + V_{\text{frac}}(t), \tag{B. 6}$$

$$V_{\text{frac}}(t) = \frac{2\pi}{\theta_0}(r_{\text{frac}}(t) - r_0)wh(t), \tag{B. 7}$$

where V_0 is the syringe volume before air injection, r_0 is the injection port radius, $V_{\text{air}}(t)$ is the air volume in the cell that consists of the air volume at the injection port and the volume of fractures $V_{\text{frac}}(t)$, w is the fracture width, and P_0 is the atmospheric pressure.

3. Assuming incompressible solid grains, conservation of mass for the solid grains states that

$$\frac{\partial V_s}{\partial t} = 0 \to \frac{\partial[(V_t(t) - V_{\text{air}}(t))\phi_{3d}]}{\partial t} = 0, \tag{B. 8}$$

where $V_t(t)$ is the total cell volume. As ϕ_{3d} is a constant with time, the equation becomes:

$$V_{\text{air}}(t) = \pi R^2(h(t) - h_0) + \pi r_0^2 h_0, \tag{B. 9}$$

where R is the radius of the cell.

4. We establish the quasi-static force balance for the top plate assuming Hertzian contacts for the granular pack. When all the particles are in contact with both the top and bottom plates ($h(t) < d$), the confining weight is balanced by contact forces between particles and plates and the integrated pore pressure force. When the top plate is lifted to $h(t) > d$, particles have contacts with either the top or bottom plate, and the vertical component (F_v) of the interparticle force (F_p) is negligible from the geometric configuration, $\frac{F_v}{F_p} = \frac{h-d}{d} < 0.03$, and thus the confining weight is balanced by the integrated pore pressure force only:

$$K_n \Big\langle (d - h(t)) \Big\rangle^{\frac{3}{2}} + P_{\text{inj}}(t)\pi r_0^2 + \frac{2\pi}{\theta_0} \int_{r_0}^{R} \int_{-\frac{\theta_0}{2}}^{\frac{\theta_0}{2}} p(r, \theta, t) r \, d\theta \, dr = W, \tag{B. 10}$$

where K_n is the contact normal stiffness of the granular pack under the confining weight.

Initial and boundary conditions

The initial conditions for the four unknowns ($P_{\text{inj}}(t)$, $h(t)$, $r_{\text{frac}}(t)$, and $p(r, \theta, t)$) are as follows:

$$P_{\text{inj}}(t = 0) = 0, \tag{B. 11}$$

$$h(t = 0) = h_0 = d - (\frac{W}{K_n})^{2/3}, \tag{B. 12}$$

$$r_{\text{frac}}(t = 0) = r_0, \tag{B. 13}$$

$$p(r_0 \leq r \leq R, -\frac{\theta_0}{2} \leq \theta \leq \frac{\theta_0}{2}, t = 0) = 0, \tag{B. 14}$$

The boundary conditions are:

$$p(R, \theta, 0) = 0, \tag{B. 15}$$

$$p(r_0 \leq r \leq r_{\text{frac}}(t), \pm\theta_0/2, t) = p(r_0, \theta, t) = P_{\text{inj}}(t), \tag{B. 16}$$

$$\frac{\partial p}{\partial \theta}\bigg|_{(r_{\text{frac}}(t) \leq r \leq R, \pm\theta_0/2, t)} = 0, \tag{B. 17}$$

Modeling parameters

A summary of the modeling parameters is shown in Table I. There is no fitting parameter in this model. The Hertzian-contact normal stiffness, K_n, is measured from a separate

TABLE I. Modeling parameters for a mechanistic model of a representative fracture wedge

Symbol	Value	Unit	Variable
r_0	2	mm	Injection port radius
R	10.6	cm	Hele-Shaw cell radius
M_s	40	g	Mass of the photoelastic particles
ρ_s	1	g/cm^3	Density of the photoelastic particles
ϕ_{3d}	0.58,0.59,0.60		3D packing density under $W = 25, 65, 85$ N
W	25,65,85	N	Confining weight acting on the the granular pack
d	2	mm	Diameter of the photoelastic particles
K_n	9.4e7	Nm$^{-3/2}$	Hertzian contact normal stiffness of the granular pack
q	100	mL/min	Air injection rate
V_0	15	mL	Air reservoir volume
P_0	101	kPa	Atmospheric pressure
θ	$\pi/3$		Angle of a representative fracture wedge
w	$3d$	mm	Fracture width
h_0	$0.98d$,$0.96d$,$0.95d$	mm	Initial height of the granular pack under $W = 25, 65, 85$ N
k	$(0.08d)^2$	mm^2	Permeability of the granular pack
k'	$d^2/12$	mm^2	Effective permeability of the granular-fluid mixture
η	9.71	Pa·s	Defending fluid viscosity
η'	9.8η	Pa·s	Effective viscosity of the granular-fluid mixture [36]

experiment where we track the vertical displacement of the top plate as the confining weight increases from 10 N to 110 N, the permeability of the granular pack, k, is measured in consolidation experiments [30]. Other parameters are either calculated from the experimental set up ($r_0, R, M_s, \rho_s, \phi_{3d}, W, d, q, V_0, P_0, h_0, k', \eta, \eta'$), or directly measured during the fracturing experiments (w, θ_0).

Numerical implementation

We use a finite difference numerical scheme to solve the four coupled governing equations [B. 4, 5, 9 and 10]. The numerical implementation scheme for the mathematical model is shown in Fig. 9. The fluid pressure is fully coupled with granular mechanics by solving the unknown variables, $h(t)$ and $r_{\mathrm{frac}}(t)$, iteratively until convergence at each time step.

* juanes@mit.edu

[1] David E Hill and J-Y Parlange, "Wetting front instability in layered soils," Soil Sci. Soc. Am. J. **36**, 697–702 (1972).

[2] Guillaume T Charras, Justin C Yarrow, Mike A Horton, L Mahadevan, and TJ Mitchison, "Non-equilibration of hydrostatic pressure in blebbing cells," Nature **435**, 365–369 (2005).

[3] Michael L Szulczewski, Christopher W MacMinn, Howard J Herzog, and Ruben Juanes, "Lifetime of carbon capture and storage as a climate-change mitigation technology," Proc. Natl. Acad. Sci. U.S.A. **109**, 5185–5189 (2012).

[4] Ruben Juanes, Yue Meng, and Bauyrzhan K Primkulov, "Multiphase flow and granular mechanics," Phys. Rev. Fluids **5**, 110516 (2020).

[5] A. Groisman and E. Kaplan, "An experimental study of cracking induced by desiccation," Europhys. Lett. **25**, 415–420 (1994).

[6] H. Shin and J. C. Santamarina, "Desiccation cracks in saturated fine-grained soils: particle-level phenomena and effective-stress analysis," Geotechnique **61**, 961–972 (2011).

[7] Eric R Dufresne, Eric I Corwin, NA Greenblatt, Jacqueline Ashmore, DY Wang, Anthony D Dinsmore, JX Cheng, XS Xie, John W Hutchinson, and David A Weitz, "Flow and fracture in drying nanoparticle suspensions," Phys. Rev. Lett. **91**, 224501 (2003).

[8] Dominic Vella, Pascale Aussillous, and L Mahadevan, "Elasticity of an interfacial particle raft," Europhys. Lett. **68**, 212 (2004).

[9] AK Jain and R Juanes, "Preferential mode of gas invasion in sediments: Grain-scale mechanistic model of coupled multiphase fluid flow and sediment mechanics," J. Geophys. Res. Solid Earth **114**, B08101 (2009).

[10] Hosung Shin and J Carlos Santamarina, "Fluid-driven fractures in uncemented sediments: Underlying particle-level processes," Earth Planet. Sci. Lett. **299**, 180–189 (2010).

[11] Lucas Goehring, William J Clegg, and Alexander F Routh, "Plasticity and fracture in drying colloidal films," Phys. Rev. Lett. **110**, 024301 (2013).

[12] Christian Peco, Wei Chen, Yingjie Liu, MM Bandi, John E Dolbow, and Eliot Fried, "Influence of surface tension in the surfactant-driven fracture of closely-packed particulate monolayers," Soft Matter **13**, 5832–5841 (2017).

[13] Zhonghao Sun and J Carlos Santamarina, "Grain-displacive gas migration in fine-grained sediments," J. Geophys. Res. Solid Earth **124**, 2274–2285 (2019).

[14] Bjornar Sandnes, HA Knudsen, KJ Måløy, and EG Flekkøy, "Labyrinth patterns in confined granular-fluid systems," Phys. Rev. Lett. **99**, 038001 (2007).

[15] Xiang Cheng, Lei Xu, Aaron Patterson, Heinrich M Jaeger, and Sidney R Nagel, "Towards the zero-surface-tension limit in granular fingering instability," Nat. Phys. **4**, 234 (2008).

[16] Haiying Huang, Fengshou Zhang, Patrick Callahan, and Joseph Ayoub, "Granular fingering in fluid injection into dense granular media in a hele-shaw cell," Phys. Rev. Lett. **108**, 258001 (2012).

[17] Fengshou Zhang, Branko Damjanac, and Haiying Huang, "Coupled discrete element modeling of fluid injection into dense granular media," J. Geophys. Res. Solid Earth **118**, 2703–2722 (2013).

[18] Bjornar Sandnes, EG Flekkøy, HA Knudsen, KJ Måløy, and H See, "Patterns and flow in frictional fluid dynamics," Nat. Commun. **2**, 288 (2011).

[19] Benjamin P Scandella, Liam Pillsbury, Thomas Weber, Carolyn Ruppel, Harold F Hemond, and Ruben Juanes, "Ephemerality of discrete methane vents in lake sediments," Geophys. Res. Lett. **43**, 4374–4381 (2016).

[20] Tad W Patzek, Frank Male, and Michael Marder, "Gas production in the barnett shale obeys a simple scaling theory," Proc. Natl. Acad. Sci. U.S.A. **110**, 19731–19736 (2013).

[21] J Mataix-Solera, V Arcenegui, N Tessler, R Zornoza, L Wittenberg, C Martínez, P Caselles, A Pérez-Bejarano, D Malkinson, and MM Jordán, "Soil properties as key factors controlling water repellency in fire-affected areas: Evidences from burned sites in spain and israel," Catena **108**, 6–13 (2013).

[22] Ran Holtzman, Michael L Szulczewski, and Ruben Juanes, "Capillary fracturing in granular media," Phys. Rev. Lett. **108**, 264504 (2012).

[23] Ran Holtzman and Ruben Juanes, "Crossover from fingering to fracturing in deformable disordered media," Phys. Rev. E **82**, 046305 (2010).

[24] Benoit Carrier and Sylvie Granet, "Numerical modeling of hydraulic fracture problem in permeable medium using cohesive zone model," Eng. Fract. Mech. **79**, 312–328 (2012).

[25] Brice Lecampion and Jean Desroches, "Simultaneous initiation and growth of multiple radial hydraulic fractures from a horizontal wellbore," J. Mech. Phys. Solids **82**, 235–258 (2015).

[26] Andro Mikelic, Mary F Wheeler, and Thomas Wick, "A phase-field method for propagating fluid-filled fractures coupled to a surrounding porous medium," Multiscale Model. Simul. **13**, 367–398 (2015).

[27] David Santillán, Ruben Juanes, and Luis Cueto-Felgueroso, "Phase field model of hydraulic fracturing in poroelastic media: Fracture propagation, arrest, and branching under fluid injection and extraction," Journal of Geophysical Research: Solid Earth **123**, 2127–2155 (2018).

[28] Yue Meng, Bauyrzhan K Primkulov, Zhibing Yang, Chung Yee Kwok, and Ruben Juanes, "Jamming transition and emergence of fracturing in wet granular media," Phys. Rev. Res. **2**, 022012 (2020).

[29] Francisco J Carrillo and Ian C Bourg, "Capillary and viscous fracturing during drainage in porous media," Phys. Rev. E **103**, 063106 (2021).

[30] Wei Li, Yue Meng, Bauyrzhan K Primkulov, and Ruben Juanes, "Photo-poromechanics: An experimental method to visualize the effective stress field in fluid-filled granular media," Phys. Rev. Appl. **16**, 024043 (2021).

[31] Jonathan Barés, Serge Mora, Jean-Yves Delenne, and Thierry Fourcaud, "Experimental observations of root growth in a controlled photoelastic granular material," in *EPJ Web of Conferences*, Vol. 140 (EDP Sciences, 2017) p. 14008.

[32] Karen E Daniels, Jonathan E Kollmer, and James G Puckett, "Photoelastic force measurements in granular materials," Rev. Sci. Instrum. **88**, 051808 (2017).

[33] Michael L Falk and James S Langer, "Dynamics of viscoplastic deformation in amorphous solids," Phys. Rev. E **57**, 7192 (1998).

[34] L Rothenburg and APS Selvadurai, "A micromechanical definition of the cauchy stress tensor for particulate media," in *Mechanics of Structural Media, Proc. of the Int. Symp. on the*

Mechanical Behaviour of Structured Media, Ottawa, Canada, 18–21 May (Elsevier, 1981) pp. 469–486.

[35] See Supplemental Material at [URL will be inserted by publisher] for videos corresponding to the conditions in Fig. 2.

[36] D Quemada, "Rheology of concentrated disperse systems and minimum energy dissipation principle," Rheol. Acta **16**, 82–94 (1977).

[37] Philip Geoffrey Saffman and Geoffrey Ingram Taylor, "The penetration of a fluid into a porous medium or hele-shaw cell containing a more viscous liquid," Proc. Math. Phys. Eng. Sci. P Roy Soc A-Math Phy. **245**, 312–329 (1958).

[38] C Chevalier, A Lindner, M Leroux, and E Clément, "Morphodynamics during air injection into a confined granular suspension," J. Non-Newton. Fluid Mech. **158**, 63–72 (2009).

[39] Corey S O'Hern, Leonardo E Silbert, Andrea J Liu, and Sidney R Nagel, "Jamming at zero temperature and zero applied stress: The epitome of disorder," Phys. Rev. E **68**, 011306 (2003).

[40] TS Majmudar, M Sperl, Stefan Luding, and Robert P Behringer, "Jamming transition in granular systems," Phys. Rev. Lett. **98**, 058001 (2007).

[41] Hernan A Makse, Nicolas Gland, David L Johnson, and Lawrence Schwartz, "Granular packings: Nonlinear elasticity, sound propagation, and collective relaxation dynamics," Phys. Rev. E **70**, 061302 (2004).

[42] Kenneth Langstreth Johnson and Kenneth Langstreth Johnson, *Contact Mechanics* (Cambridge university press, 1987).

[43] Pijush K Kundu, Ira M Cohen, and D Dowling, *Fluid Mechanics* (Elsevier, 2008).

[44] Corey S O'Hern, Stephen A Langer, Andrea J Liu, and Sidney R Nagel, "Random packings of frictionless particles," Phys. Rev. Lett. **88**, 075507 (2002).

[45] Leonardo E Silbert, Deniz Ertaş, Gary S Grest, Thomas C Halsey, and Dov Levine, "Geometry of frictionless and frictional sphere packings," Phys. Rev. E **65**, 031304 (2002).

[46] Christopher W MacMinn, Eric R Dufresne, and John S Wettlaufer, "Fluid-driven deformation of a soft granular material," Phys. Rev. X **5**, 011020 (2015).

[47] Claus Heussinger and Jean-Louis Barrat, "Jamming transition as probed by quasistatic shear flow," Phys. Rev. Lett. **102**, 218303 (2009).

[48] James G Berryman, "Random close packing of hard spheres and disks," Phys. Rev. A **27**, 1053 (1983).

[49] Massimo Pica Ciamarra, Raffaele Pastore, Mario Nicodemi, and Antonio Coniglio, "Jamming phase diagram for frictional particles," Phys. Rev. E **84**, 041308 (2011).

[50] Ning Xu, Jerzy Blawzdziewicz, and Corey S O'Hern, "Random close packing revisited: Ways to pack frictionless disks," Phys. Rev. E **71**, 061306 (2005).

[51] DM Wendell, K Luginbuhl, J Guerrero, and AE Hosoi, "Experimental investigation of plant root growth through granular substrates," Exp. Mech. **52**, 945–949 (2012).

[52] Kevin Kendall and Carl Stainton, "Adhesion and aggregation of fine particles," Powder Technol. **121**, 223–229 (2001).

[53] John Conrad Jaeger, Neville GW Cook, and Robert Zimmerman, *Fundamentals of Rock Mechanics* (John Wiley & Sons, 2009).

[54] James Kenneth Mitchell and Kenichi Soga, *Fundamentals of Soil Behavior*, Vol. 3 (John Wiley & Sons New York, 2005).

[55] Donald L Turcotte, Eldridge M Moores, and John B Rundle, "Super fracking," Phys. Today **67**, 34 (2014).

[56] Ebrahim Ghanbari and Hassan Dehghanpour, "The fate of fracturing water: A field and simulation study," Fuel **163**, 282–294 (2016).

[57] Adam Skarke, Carolyn Ruppel, M Kodis, D Brothers, and E Lobecker, "Widespread methane leakage from the sea floor on the northern us atlantic margin," Nat. Geosci. **7**, 657–661 (2014).

[58] A. L. Handwerger, A. W. Rempel, R. M. Skarbek, J. J. Roering, and G. E. Hilley, "Rate-weakening friction characterizes both slow sliding and catastrophic failure of landslides," Proc. Natl. Acad. Sci. U.S.A. **113**, 10281–10286 (2016).

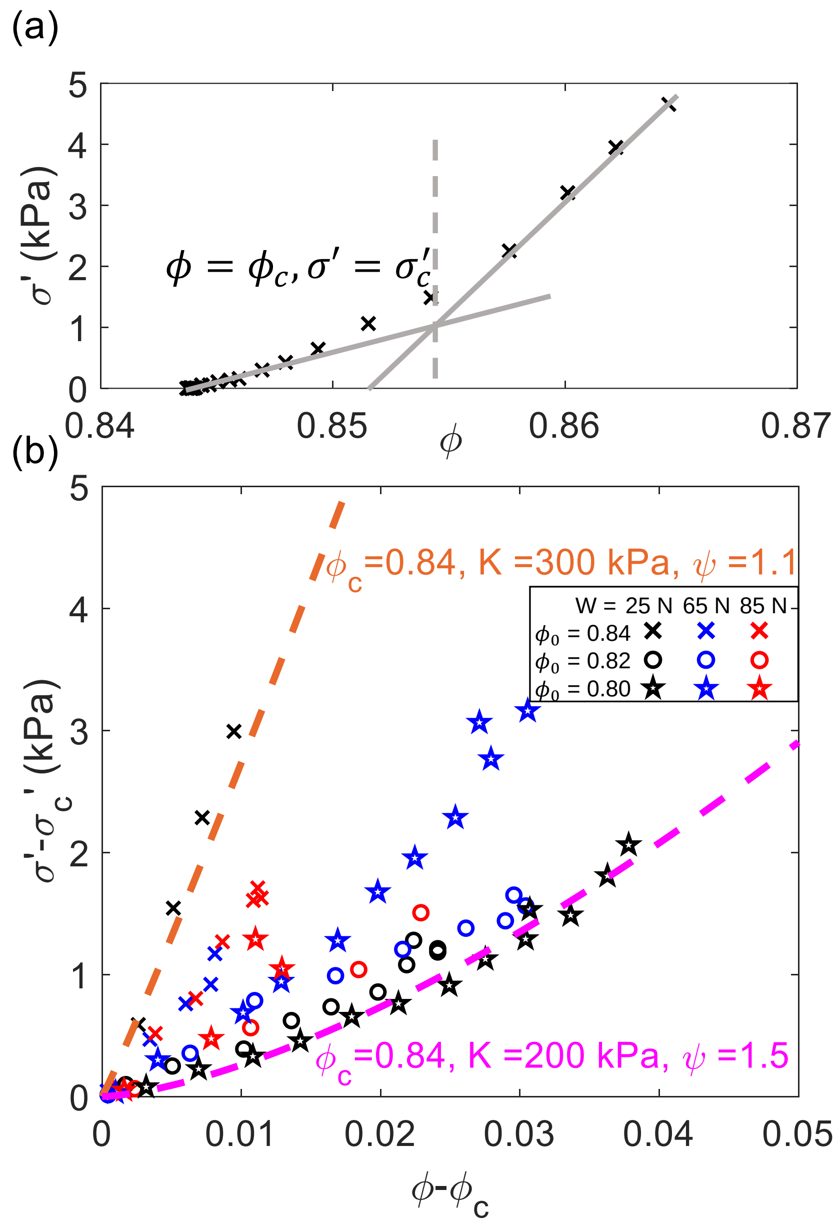

FIG. 6. Jamming transition analysis for the fracturing experiments (ϕ_0 =0.84, 0.82, 0.80, W = 25 N, 65 N, 85 N). (a) Determination of the critical packing density and effective stress at jamming for the experiment W = 25 N, ϕ_0 = 0.84. (b) $\sigma' - \sigma'_c$ plotted against $\phi - \phi_c$ for the fracturing experiments, which follows the power-law constitutive relationship $\sigma' - \sigma'_c = K\left\langle \frac{\phi-\phi_c}{\phi_c} \right\rangle^{\psi}$ [39, 40, 44–46].

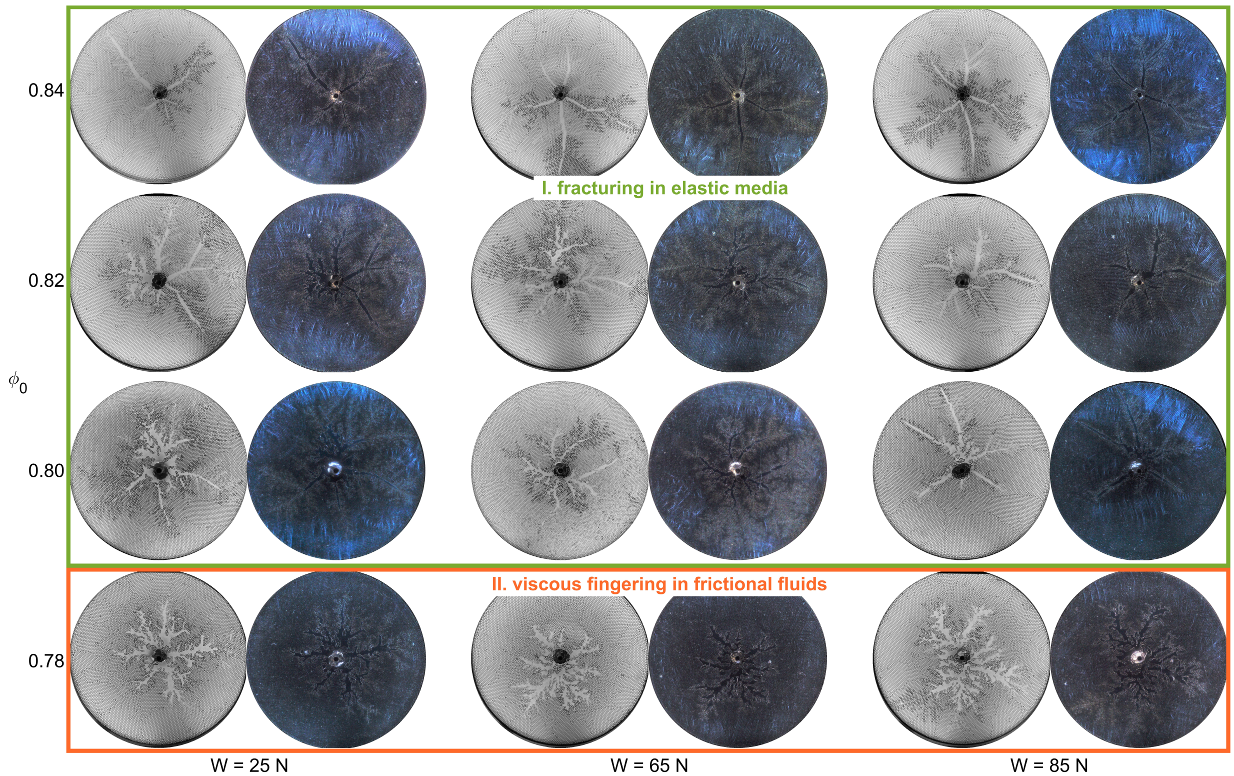

FIG. 7. Visual phase diagram of the bright-field (left) and dark-field (right) invading fluid morphology at breakthrough corresponding to different confining weights W and initial packing densities ϕ_0. From dark-field images that visualize the effective stress field, the invading morphology and rheology of the granular packs is classified as fracturing in fluid-filled elastic media (with strong photoelastic response, $\phi_0 = 0.84, 0.82, 0.80$), or viscous fingering in frictional fluids (with weak or negligible photoelastic response, $\phi_0 = 0.78$). Behind the propagating fracture tips, the effective stress field exhibits an evolving "effective stress shadow", where the intergranular stress is low and the granular pack exhibits undrained behavior.

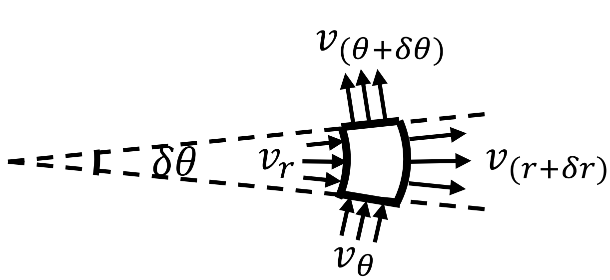

FIG. 8. An annulus sector used to derive the pressure diffusion equation in radial coordinates.

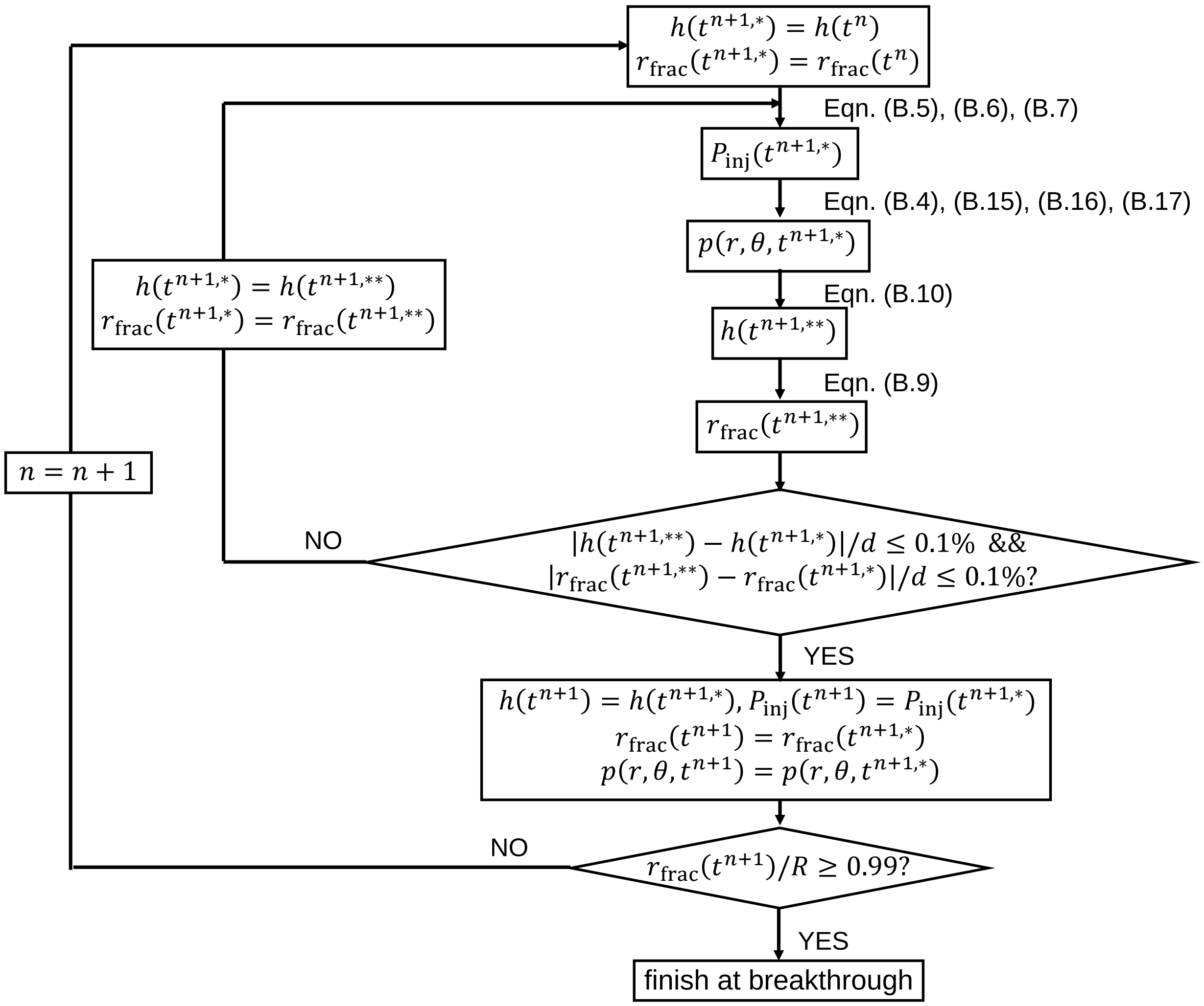

FIG. 9. Numerical implementation scheme for the mathematical model. The fluid pressure is fully coupled with granular mechanics by solving the unknown variables, $h(t)$ and $r_{\mathrm{frac}}(t)$, iteratively until convergence at each time step.